

Zonal Variations in the Southern Ocean Heat Budget

VERONICA TAMSITT, LYNNE D. TALLEY, MATTHEW R. MAZLOFF,
AND IVANA CEROVEČKI

Scripps Institution of Oceanography, La Jolla, California

(Manuscript received 3 September 2015, in final form 4 June 2016)

ABSTRACT

The spatial structure of the upper ocean heat budget in the Antarctic Circumpolar Current (ACC) is investigated using the $\frac{1}{6}^\circ$, data-assimilating Southern Ocean State Estimate (SOSE) for 2005–10. The ACC circumpolar integrated budget shows that 0.27 PW of ocean heat gain from the atmosphere and 0.38 PW heat gain from divergence of geostrophic heat transport are balanced by -0.58 PW cooling by divergence of Ekman heat transport and -0.09 PW divergence of vertical heat transport. However, this circumpolar integrated balance obscures important zonal variations in the heat budget. The air–sea heat flux shows a zonally asymmetric pattern of ocean heat gain in the Indian and Atlantic sectors and ocean heat loss in the Pacific sector of the ACC. In the Atlantic and Indian sectors of the ACC, the surface ocean heat gain is primarily balanced by divergence of equatorward Ekman heat transport that cools the upper ocean. In the Pacific sector, surface ocean heat loss and cooling due to divergence of Ekman heat transport are balanced by warming due to divergence of geostrophic heat advection, which is similar to the dominant heat balance in the subtropical Agulhas Return Current. The divergence of horizontal and vertical eddy advection of heat is important for warming the upper ocean close to major topographic features, while the divergence of mean vertical heat advection is a weak cooling term. The results herein show that topographic steering and zonal asymmetry in air–sea exchange lead to substantial zonal asymmetries in the heat budget, which is important for understanding the upper cell of the overturning circulation.

1. Introduction

The Southern Ocean component of the global meridional overturning circulation is fundamentally important to climate through air–sea exchange and redistribution of heat, freshwater, carbon, and nutrients (e.g., [Sarmiento et al. 2004](#); [Ito et al. 2010](#)). Westerly winds drive the eastward flowing Antarctic Circumpolar Current (ACC), linking the major ocean basins and allowing interbasin exchange of properties. The circumpolar nature of the Southern Ocean and predominately zonal flow of the ACC have led to frequent use of zonally averaged theories to describe the Southern Ocean overturning circulation. Residual-mean theories explain the circumpolar-mean overturning circulation as a balance between the northward Eulerian transport driven by wind forcing and an opposing southward eddy-driven transport (e.g.,

[Karsten and Marshall 2002](#); [Marshall and Radko 2003](#)). However, a zonally averaged view of the Southern Ocean is limited because interaction of the flow with topography and asymmetries in air–sea exchange lead to zonal asymmetries in Southern Ocean dynamics and properties, including zonal geostrophic heat transport ([Sun and Watts 2002](#)), eddy kinetic energy ([Chelton et al. 1990](#)), response of the mixed layer depth to wind variability ([Sallée et al. 2010](#)), and cross-front particle exchange ([Thompson and Sallée 2012](#)).

The isopycnals in the ACC are steeply tilted upward toward Antarctica and outcrop at the surface allowing upwelling of deep, dense water, which influences air–sea exchange. Surface buoyancy gain over the Southern Ocean is necessary to convert these upwelled water masses to lighter water masses at the surface and is important for setting the strength of the upper cell of the meridional overturning circulation ([Radko and Marshall 2006](#); [Morrison et al. 2011](#)). Freshwater flux dominates the total surface buoyancy flux poleward of the ACC and heat flux dominates equatorward of the ACC, while in the ACC latitude range both heat flux and freshwater flux contribute to buoyancy flux ([Speer et al. 2000](#); [Iudicone](#)

Corresponding author address: Veronica Tamsitt, Climate, Atmospheric Science and Physical Oceanography, Scripps Institution of Oceanography, UC San Diego, 9500 Gilman Dr., La Jolla, CA 92093-0230.

E-mail: vtamsitt@ucsd.edu

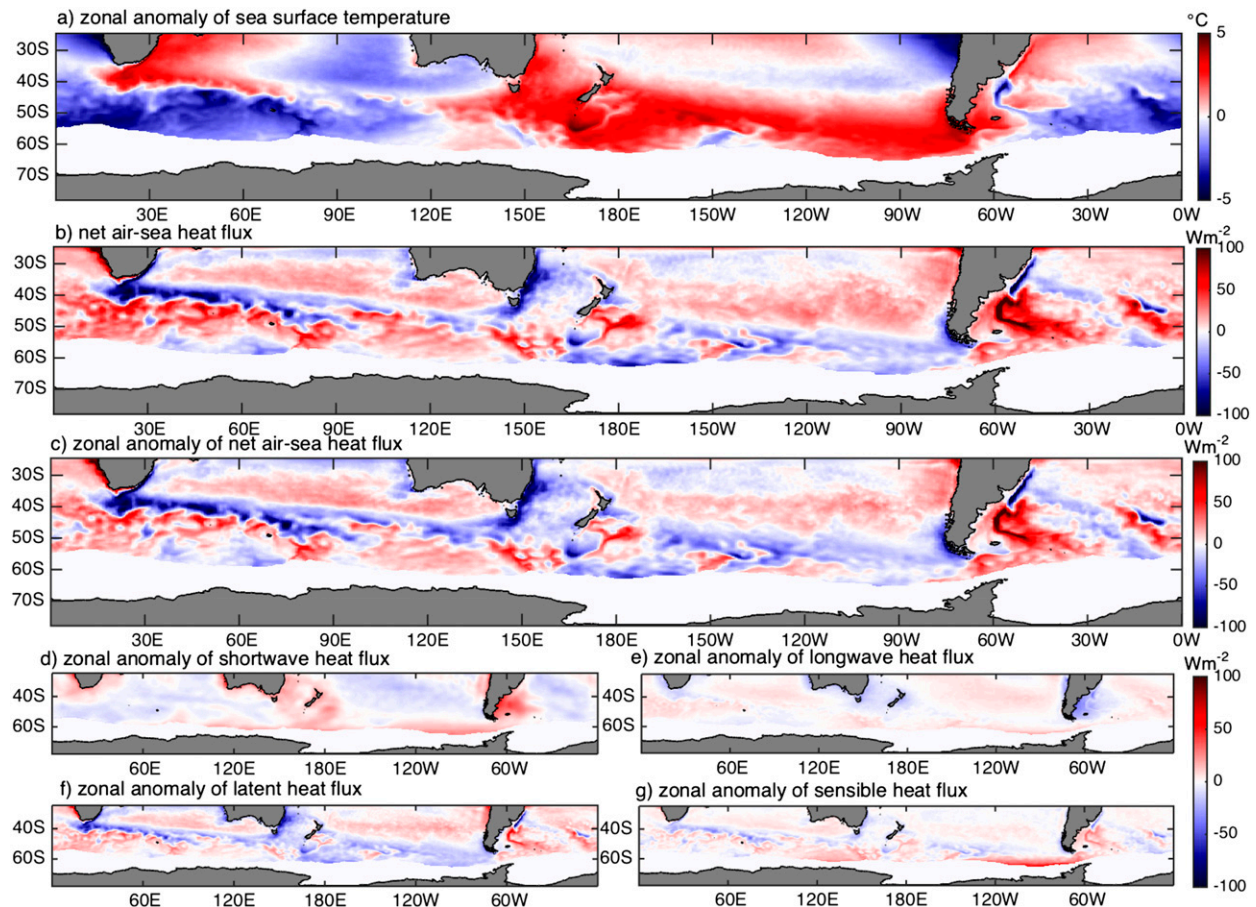


FIG. 1. SOSE 2005–10 mean of (a) zonal anomaly of sea surface temperature ($^{\circ}\text{C}$), (b) net air-sea heat flux (W m^{-2} ; with positive defined as heat flux into the ocean), (c) zonal anomaly of net air-sea heat flux, (d) zonal anomaly of net shortwave heat flux, (e) zonal anomaly of net longwave radiation (incoming – outgoing), (f) zonal anomaly of net latent heat flux, and (g) zonal anomaly net sensible heat flux. We have masked the temperature and fluxes in the region south of the 2005–10 annual mean sea ice boundary where the fluxes are significantly influenced by sea ice as this region will not be considered in this analysis.

et al. 2008; Cerovečki et al. 2013). Air-sea heat flux shows large spatial inhomogeneity in the ACC; as a result, heat fluxes are a major contribution to the impact of buoyancy fluxes on the overturning circulation in the ACC. However, our knowledge about air-sea fluxes has been severely limited due to a lack of direct observations (Bourassa et al. 2013), and air-sea heat fluxes have been identified as the largest contributor to uncertainty in the upper ocean heat budget (Dong et al. 2007; Faure et al. 2011).

Recently developed air-sea flux products that constrain the heat fluxes with additional observations and reduce the global long-term surface heat imbalance (Large and Yeager 2009) as well as adjusted fluxes from state estimates constrained to observations (Figs. 1a,b) show agreement in large-scale patterns of air-sea heat fluxes in the Southern Ocean (Cerovečki et al. 2011). These improved heat flux products reveal a robust, large-scale zonally asymmetric pattern in the ACC of broad

ocean heat gain in the Indian and Atlantic basins and a broad region of ocean cooling in the Pacific basin (Fig. 1b). The impact of this zonal dipole on the overturning circulation has been explored in an idealized model (Radko and Marshall 2006), showing a stronger residual overturning circulation in the region of larger buoyancy gain due to stronger ocean heat gain in the Indian and Atlantic sectors. From in situ ocean observations, Sun and Watts (2002) show that the ACC warms where it flows equatorward in the Atlantic and Indian sectors, and cools where it flows poleward in the Pacific sector. The zonal dipole air-sea heat flux pattern in Fig. 1 matches their inference of warming and cooling, although the Southern Ocean State Estimate (SOSE) and Large and Yeager's (2009) heat flux pattern are zonally much broader than in the proposal by Sun and Watts (2002).

Dong et al. (2007) used observations and a simple model to estimate the mixed layer heat budget in the

Southern Ocean from 40° to 60°S and inferred that in the domain average and in each basin the dominant mixed layer balance is between air–sea heat gain and cooling by divergence of meridional Ekman advection of temperature, and that divergence of geostrophic advection of temperature plays a minimal role. This balance between air–sea heat fluxes and divergence of Ekman heat advection differs significantly from western boundary current regions, where poleward geostrophic advection of warm subtropical water is important in balancing ocean heat loss to the atmosphere in the mixed layer (Vivier et al. 2002; Dong and Kelly 2004; Roemmich et al. 2005). Quasi-northward Ekman transport has been identified as the dominant cooling mechanism in the ACC upper ocean and is important for Subantarctic Mode Water formation (Sloyan and Rintoul 2001; Rintoul and England 2002; Sallée et al. 2006, 2008). Recent work has suggested significant differences in the mixed layer heat balance in different zones north of, south of, and within the ACC fronts (Sallée et al. 2008; Faure et al. 2011), and shown that regional heat balances depart from the zero-order balance between air–sea flux and Ekman heat transport, highlighting the importance of topography and mesoscale processes on the evolution of upper ocean temperature (Sallée et al. 2008; Vivier et al. 2010). Lateral eddy heat diffusion has been shown to contribute to substantial warming locally and is strongest downstream of major topographic features but vanishes with large-scale averaging (Sallée et al. 2008). Seasonal variability in the mixed layer heat budget is dominated by strong seasonal variability in the air–sea heat flux (Dong et al. 2007; Sallée et al. 2006) although Ekman temperature advection also shows seasonal variability (Dong et al. 2007). Temperature tendency variance in the ACC mixed layer has been shown to be dominated by lateral advection, including both higher-frequency transient eddies and lower-frequency meanders (Vivier et al. 2010).

Previous observation-based heat budget calculations use simple mixed layer models that neglect important vertical physics due to a lack of sufficient subsurface observations (Vivier et al. 2010) and cannot completely close the heat budget primarily due to uncertainties in the air–sea flux datasets (Dong et al. 2007). The detailed spatial variability of the heat budget in the Southern Ocean is thus mostly unknown, particularly how the budget differs between regions with net air–sea heat gain and regions of air–sea heat loss. Eddy heat fluxes have been shown to be important in regions of the ACC (e.g., Sallée et al. 2006) but limited observations have made it difficult to diagnose the eddy contribution to the heat budget equation. Increased model resolution and improvement of ocean data assimilation techniques

have prompted the development of eddy-permitting, multiyear state estimates of the ocean (e.g., Mazloff et al. 2010; Wunsch and Heimbach 2013). A distinct advantage of analyzing the heat budget in a high-resolution, data-assimilating state estimate such as the Southern Ocean State Estimate is that the mass and heat budgets are closed at every grid point and vertical advective and diffusive processes are explicitly resolved or parameterized in the model. Additionally, numerous ocean observations in state estimates constrain the large-scale upper ocean state so that the model representation of upper ocean stratification is consistent with observations, making it possible to explore the three-dimensional heat budget within the upper ocean.

The goal of this study is to examine the effects of ocean dynamics in the regions of ocean heat gain and loss along the ACC on the heat budget in the eddy-permitting, data-assimilating SOSE. This Southern Ocean heat budget analysis using SOSE is timely and novel because of the improvement in air–sea fluxes through ocean state estimation compared with atmospheric reanalyses (Cerovečki et al. 2011) and the ability to fully close the heat budget at every grid point. Additionally, analysis of the upper ocean heat budget will provide insight into the role of surface heat flux as a component of buoyancy flux in setting the three-dimensional structure and strength of the upper cell of the Southern Ocean meridional overturning circulation. In section 2 we describe the model and methods used in calculating the heat budget. The adjusted air–sea heat fluxes in the model are discussed in section 3, and the heat budget and spatial and seasonal variability are analyzed in section 4. The results and conclusions are summarized in section 5.

2. Model and methods

a. The Southern Ocean State Estimate

The SOSE (Mazloff et al. 2010) is an eddy-permitting, data-assimilating model developed using software developed by the consortium for Estimating the Climate and Circulation of the Ocean (ECCO; <http://www.ecco-group.org>). The SOSE ocean dynamics is represented using the Massachusetts Institute of Technology general circulation model (MITgcm; Marshall et al. 1997). The configuration of the model used here has 1° horizontal resolution and 42 vertical levels in the domain from 24.7° to 78°S with an open northern boundary and a 900-s time step and subgrid parameterizations as described in Mazloff et al. (2010). Using an adjoint method, the model is fitted to the majority of available observations in the Southern Ocean to minimize the squared

difference between the model and observations iteratively by adjusting the “control vector” that consists of the initial conditions and atmospheric state. The initial and northern open boundary conditions are from a 1° global state estimate (Forget 2010) and the initial atmospheric state is constrained by the ECMWF ERA-Interim global reanalysis (Dee et al. 2011). Momentum, heat, and freshwater fluxes between the atmosphere and ocean are determined using bulk formulas (Large and Yeager 2009). The thermodynamic sea ice model is similar to that described by Fenty and Heimbach (2013) and includes albedo as a function of surface ice conditions and turbulent air–ice fluxes calculated using standard bulk aerodynamic formulas. The SOSE solution has been extensively validated and compared to observations (e.g., Cerovečki et al. 2013). The SOSE adjusted air–sea fluxes have been validated against other

available flux products and are consistent with the best modern flux estimates (Cerovečki et al. 2011). As expected, the largest differences between SOSE and other flux products tend to be in regions with strong mesoscale activity such as the ACC and western boundary currents.

b. Heat budget analysis

The SOSE iteration 100 solution used for this analysis is a 6-yr (2005–10) updated version of the solution described by Mazloff et al. (2010). Terms in the heat and salt budgets are diagnosed at each grid point from the model state and output as 5-day averages. The time evolution of temperature in the ocean is given by the sum of net heat exchange with the atmosphere, divergence of advective heat transport by geostrophic horizontal, ageostrophic horizontal, and vertical velocities, and three-dimensional diffusive processes:

$$\underbrace{\frac{\partial T}{\partial t}}_{\text{temperature tendency}} = \underbrace{\frac{Q(z)}{\rho c_p dz}}_{\text{air-sea flux}} - \underbrace{\mathbf{u}_g \cdot \nabla_H T}_{\text{geostrophic advection}} - \underbrace{\mathbf{u}_a \cdot \nabla_H T}_{\text{ageostrophic advection}} - \underbrace{w \cdot \frac{\partial T}{\partial z}}_{\text{vertical advection}} + \underbrace{\kappa_H \nabla_H^2 T + \kappa_z \frac{\partial^2 T}{\partial z^2} + K_T^{\text{turb}}}_{\text{diffusion}}, \quad (1)$$

where T is potential temperature, $\partial T/\partial t$ is the temperature tendency, Q is the net air–sea heat flux (W m^{-2} ; positive is heat flux into the ocean) that includes depth-dependent shortwave radiation distributed vertically over several upper model layers, ρ is the density, c_p is the specific heat capacity of seawater, dz is the thickness of the model layer over which Q is distributed, \mathbf{u}_g and \mathbf{u}_a are the geostrophic and ageostrophic horizontal velocity vectors, respectively, ∇_H is the horizontal divergence operator, w is the vertical velocity, κ_H and κ_z are the horizontal and vertical diffusivity respectively, and K_T^{turb} is the K -profile parameterization (KPP) turbulent vertical diffusion term (Large et al. 1994). The KPP turbulent diffusion includes both vertical diffusion term and nonlocal transport to represent convective mixing; the two tend to oppose each other in the surface boundary layer. In SOSE, penetration of downward shortwave radiation below the surface is based on an assumption of exponential decay with depth (Paulson and Simpson 1977), following Jerlov (1968):

$$Q(z) = Q(0) \left[R \exp\left(\frac{z}{\gamma_1}\right) + (1 - R) \exp\left(\frac{z}{\gamma_2}\right) \right], \quad (2)$$

where $Q(0)$ is the downward shortwave radiation at the sea surface, z is depth, and R , γ_1 , and γ_2 are constants for water type IB as defined by Jerlov (1968). Shortwave radiation typically decays to 10% of its surface value in

the upper 25 m and to below 1% by 75 m, so the heat budget solution is only significantly affected by the choice of water type in the upper 50 m. Geostrophic velocities were calculated for this analysis from the model hydrostatic pressure, and ageostrophic velocities were calculated here as the residual between the model velocity and calculated geostrophic velocity. Geostrophic horizontal advection and vertical advection were further decomposed into time-mean and transient eddy advection terms,

$$\overline{u'_g T'} = \overline{u_g T} - \overline{u_g} \overline{T} \quad \text{and} \quad (3)$$

$$\overline{w' T'} = \overline{w T} - \overline{w} \overline{T}, \quad (4)$$

where overbars denote a 3-month seasonal mean and primes denote a deviation from this seasonal mean in the 6-yr model run. This eddy definition is chosen based on the decorrelation time scale of 34 days in the ACC estimated from altimeter data by Gille and Kelly (1996).

For brevity, each of the terms in Eq. (1) will be referred to using the label indicated on the equations. For example, divergence of geostrophic temperature transport will be referred to simply as the geostrophic advection term. In the analysis the heat budget will be examined in two ways. First, horizontal maps of the heat budget terms in Eq. (1) vertically integrated over the upper ocean are presented to show major spatial

patterns. Second, to focus more closely on zonal variations in the heat budget, every model grid point is integrated meridionally between ACC streamlines and vertically over the upper ocean. Identifying a robust streamline in the ACC is difficult due to the non-stationary and segmented fronts of the ACC but we choose to define streamlines using sea surface height (SSH) contours following numerous previous studies (e.g., Sokolov and Rintoul 2009). The upper boundary of integration is the ocean surface and the lower boundary is 624 m, which is the model layer depth that includes the deepest winter mixed layers. This depth encompasses the top 20 model layers and below this level the spatially averaged temperature variance is greatly reduced. The heat budget terms are integrated to a constant depth level rather than to an isopycnal surface, as this method simplifies the analysis and volume is conserved. Modest adjustments to the depth of the lower boundary have little influence on the conclusions presented here.

3. Heat budget

a. Time-mean air–sea heat flux

The most prominent feature of the net time-mean air–sea heat flux in the SOSE solution is the intense cooling associated with the western boundary current regions, particularly the Agulhas Return Current (ARC) flowing eastward across the Indian Ocean east of South Africa (Fig. 1b). South of these heat loss regions in the Atlantic and Indian basins, between Drake Passage (DP) at 60°W and Campbell Plateau (CP) at 170°E, is a broad region of ocean heat gain at ACC latitudes that is strongest in the northern extension of the ACC at the Malvinas Current and south of the ARC in the Indian sector. In contrast to the rest of the ACC, the Pacific Ocean sector, from CP east to DP, is dominated by weak net surface ocean heat loss, although in a given year the annual-mean heat flux can be weakly positive or negative. The broad-scale coherent patterns of heat gain and heat loss in SOSE are consistent with other recent air–sea heat flux products (Large and Yeager 2009; Cerovečki et al. 2011). SOSE additionally shows mesoscale variations in heat fluxes due to adjustments to the oceanic observations. For the remainder of this paper, “Atlantic/Indian” refers to the Southern Ocean sector bounded on the west by DP and east by CP, and “Pacific” refers to the remaining section of the Southern Ocean. We argue that considering these two sectors of the ACC based on topographic features is more appropriate to the dynamics and air–sea exchanges in the circumpolar Southern Ocean than considering the three major basins typically used.

The spatial pattern in the SOSE net air–sea heat flux zonal anomaly (Fig. 1c) is dominated by latent heat flux

(Fig. 1f) and less so by the sensible heat flux (Fig. 1g). Shortwave (Fig. 1d) and longwave (Fig. 1e) components show relatively small spatial variation, apart from a meridional gradient, and tend to compensate one another. Sensible heat flux depends directly on the air–sea temperature difference ΔT while latent heat flux depends indirectly on ΔT through the influence of temperature on the air–sea humidity difference Δq (e.g., Large and Yeager 2009). Wind speed also modulates the strength of these turbulent fluxes but is not the dominant control as wind speed can act to amplify the flux but requires the presence of a temperature or humidity gradient. Therefore, latent and sensible heat fluxes tend to respond to spatial patterns and variability in sea surface temperature (SST) (Yu and Weller 2007) and to spatial patterns in atmospheric temperature. The SOSE time mean zonal anomaly of SST (Fig. 1a) is dominated by a dipole with colder SST in the Atlantic/Indian and warmer SST in the Pacific, which is remarkably similar to the pattern in air–sea flux. Similar to SST and net air–sea heat flux, atmospheric temperature also shows a zonally asymmetric pattern, with the quasi-stationary zonal wave 1, defined as the first zonal harmonic of the geopotential height field, accounting for up to 90% of the Southern Hemisphere mean spatial distribution in atmospheric pressure (van Loon and Jenne 1972; Hobbs and Raphael 2010). Milliff et al. (1999) suggested that the zonal wave 1 pattern may represent a coupled ocean–atmosphere mode, and Hobbs and Raphael (2007) find statistically significant correlations between SST and atmospheric zonal wave 1 throughout much of the Southern Ocean.

b. Time-mean heat budget

In all regions of the Southern Ocean the dominant heat balance, integrated vertically over the upper 624 m, is between air–sea flux (Fig. 2a) and the total divergence of temperature advection (Fig. 2b), while diffusion is negligible. Individually considered geostrophic, ageostrophic, and vertical advection terms locally display strong spatial inhomogeneity with positive and negative values an order of magnitude larger than the air–sea flux values, which cancel in the sum, particularly in ACC latitudes and western boundary current regions that have high eddy kinetic energy. The geostrophic advection term (Fig. 2c) tends to be positive (increasing temperature) in the western boundary currents and ACC latitudes and is negative in the subtropical gyres where there are equatorward flows and a strong meridional temperature gradients.

The ageostrophic advection term (Fig. 2d) is negative through most of the domain, decreasing the temperature, due to Ekman transport driven by westerly winds

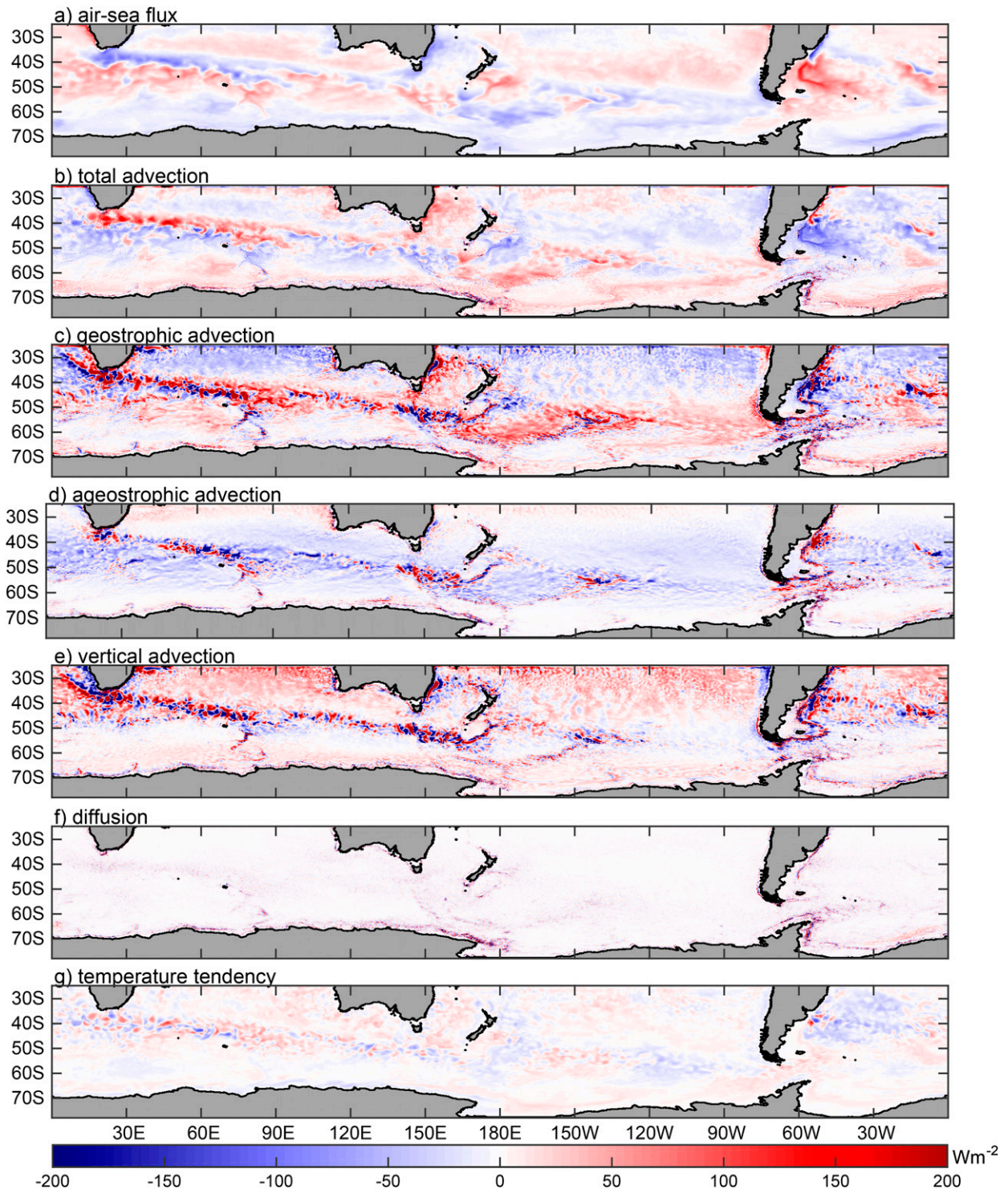


FIG. 2. SOSE 2005–10 mean heat budget terms (W m^{-2}) from Eq. (1), integrated over the upper 624 m. The (a) air–sea flux is largely balanced by (b) the total divergence of temperature advection, which is the sum of the total (c) geostrophic horizontal, (d) ageostrophic horizontal, and (e) vertical components of advection. Also shown are the (f) diffusion and (g) temperature tendency terms. Positive (red) is warming and negative (blue) is cooling.

bringing cold water equatorward. Ekman transport calculated from SOSE wind stress accounts for $> 90\%$ of the variance in ageostrophic transport in most locations. Differences between Ekman transport and ageostrophic advection are localized close to shallow topography and in regions with high eddy variability (Fig. A1). In these locations, we expect ageostrophic processes other than Ekman transport to be important at scales smaller than the Rossby radius of deformation (Rocha et al. 2016). These scales are at the limit of the smallest scales that are resolved in SOSE (Chelton et al. 1998). However, the integrated contribution of these non-Ekman ageostrophic transports to the total ageostrophic transport is negligible (Mazloff et al. 2010) (see the appendix for more details).

The vertical advection term (Fig. 2e) is generally positive (heating the upper ocean) in subtropical regions due to downwelling driven by Ekman pumping associated with wind stress curl. It is also positive along the Antarctic continental shelf where the vertical temperature gradient is reversed with colder water at the surface and relatively warm water upwelling from below. Within the ACC, but outside of locations with high eddy activity, the vertical advection term is negative (cooling) as upwelling brings colder waters toward the surface.

Integrated vertically over the upper 624 m, the diffusion term (Fig. 2f) is negligible except in deep water formation regions along the Antarctic coast that are not considered in this analysis. Although diffusion is small in the depth-integrated budget, diffusion is an important term in the mixed layer and is responsible for a large vertical redistribution of heat near the surface. The diffusion is strong within the upper 100–200 m in most locations and positive and negative signals cancel when vertically integrated to depths below the mixed layer.

The temperature tendency (Fig. 2g) is small as air–sea heat flux is largely balanced by total divergence of temperature transport (Figs. 2a,b), although it shows some large-scale spatial patterns. Given that the model run spans only 6 years, the temperature tendency patterns are most likely due to interannual variability rather than a long-term trend. The temperature tendency in Argo gridded data over the same time period shows similar spatial structure but is of somewhat smaller magnitude than in SOSE, which may be due to small model drift. However, the magnitude of the temperature tendency trend from 2005 to 2010 is small relative to the total temperature variability.

Compared to the mean ($\bar{\mathbf{u}}_g \cdot \nabla_H \bar{T}$; Fig. 3a), the eddy ($\mathbf{u}'_g \cdot \nabla_H T'$; Fig. 3b), component of the geostrophic advection term is small except in regions with high eddy variability in western boundary currents and in the ACC, where it is of a similar magnitude to the mean

geostrophic advection term. In particular, divergence of eddy heat flux is large near major topographic features including Kerguelen Plateau (60° – 80° E), Macquarie Ridge (150° E), and the Pacific–Antarctic Ridge (150° W) as well as CP and DP (Fig. 3b), consistent with observed enhancement of eddy kinetic energy and cross-frontal transport in these regions (Chelton et al. 1990; Thompson and Sallée 2012).

The mean component of the vertical advection term [$\bar{w}(\partial \bar{T}/\partial z)$; Fig. 3c], dominates the total vertical advection term outside of the energetic western boundary currents and ACC. Close to Kerguelen Plateau, at the Pacific–Antarctic Ridge, and east of DP, the mean vertical advection term is strongly negative (Fig. 3c), while the eddy component of the vertical advection term [$w'(\partial T'/\partial z)$; Fig. 3d], is positive; hence there is strong compensation between the mean and eddy components in these locations (Figs. 3c,d). The spatial pattern in the vertical eddy advection term (Fig. 3d) is similar to that of the eddy component of the geostrophic advection term (Fig. 3b) and is positive in most regions, suggesting that this eddy term represents the vertical component of along-isopycnal eddy heat flux, which leads to warming by upward eddy flux along poleward tilted isopycnals with an along-isopycnal temperature gradient (Wolfe et al. 2008).

Figure 4b shows the vertically integrated terms that are mapped in Fig. 2, also integrated meridionally within the ACC. ACC boundaries are defined as the outermost time-mean SSH lines that are closed through DP (Fig. 4a). Large-magnitude, small-scale variations are apparent in the advection terms that are concentrated in “hot spots” close to coastlines and shallow topography and in eddy-rich regions that dominate the larger-scale signals (Fig. 4b).

To more clearly visualize how each heat budget term varies as a function of longitude, the vertically and meridionally integrated terms (Fig. 4b) are cumulatively summed with longitude (Fig. 4c). There is net ocean heat gain of 0.27 PW in the circumpolar integral although the pattern of air sea heat gain in the Atlantic/Indian sector and air–sea heat loss in the Pacific is apparent. As in Fig. 2, the total geostrophic advection is generally negative or negligible in the Atlantic/Indian sector and positive throughout the Pacific sector of the ACC, with the exception of a region from 70° to 100° E in the Indian sector, downstream of Kerguelen Plateau, and 0° – 30° W, at the Brazil–Malvinas Confluence where it is also positive. This localized region of convergence of geostrophic heat advection downstream of Kerguelen Plateau is likely due to warm, subtropical ARC waters crossing the Subantarctic Front southward into the ACC downstream of Kerguelen Plateau (Wang et al. 2014).

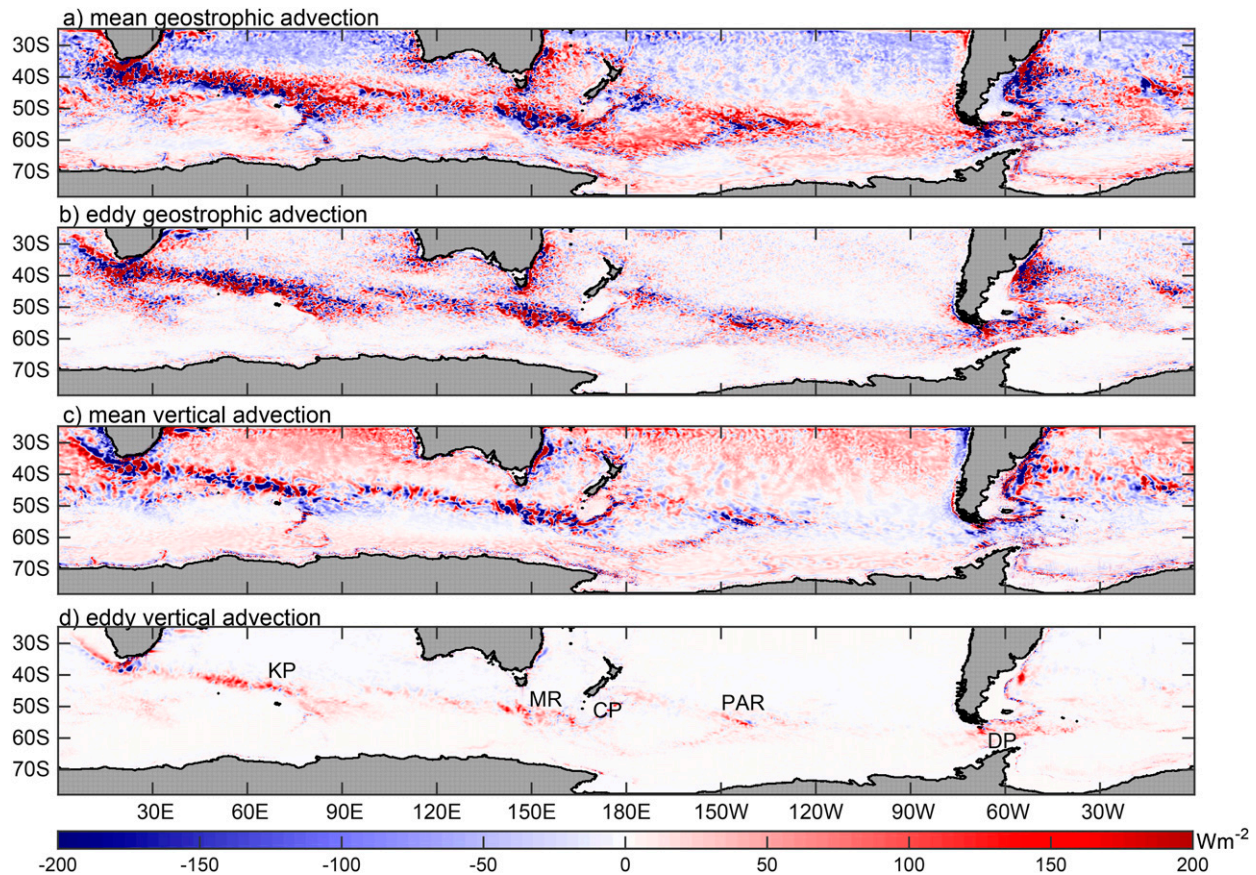


FIG. 3. As in Fig. 2, but for the time-mean and eddy components of horizontal geostrophic and vertical advection (W m^{-2}). The topographic features labeled in (d) are, from left to right, the Kerguelen Plateau (KP), Macquarie Ridge (MR), Campbell Plateau (CP), Pacific–Antarctic Ridge (PAR), and Drake Passage (DP).

Similarly, downstream of Drake Passage the positive geostrophic advection term can be attributed to cross-frontal flow of subtropical Brazil Current waters into the ACC. Again, the ageostrophic advection is consistently negative at all longitudes along the ACC associated with northward Ekman transport of colder water (Fig. A1). The total vertical advection has a weak net cooling effect, with localized contributions at major topographic features implying topographic control of vertical heat exchange (Fig. 4c). The cumulative sum of temperature tendency shows that small positive and negative temperature trends, when summed cumulatively along the ACC, are a reassuringly small contribution to the heat budget. The cumulatively summed diffusion is negligible (Fig. 4c).

Decomposition of the horizontal geostrophic and vertical advection components into contributions from the mean flow and transient eddies (Fig. 4d) shows that both horizontal and vertical eddy heat flux divergence are warming the upper ocean. This warming by eddy heat flux divergence is confined to localized regions,

predominantly in the Kerguelen Plateau region where warm ARC waters reach the ACC and, to a lesser extent, the Macquarie Ridge. In the circumpolar integral, the mean and eddy components of the geostrophic advection term are of similar magnitude. However, the mean geostrophic advection term (Fig. 4d) is responsible for the majority of the zonal variation observed in the total geostrophic advection term (Fig. 4c). There is substantial cancellation between the mean and eddy components of the vertical advection term leading to weak net cooling by the total vertical advection term that is consistent with previous modeling studies of vertical heat flux (Wolfe et al. 2008; Morrison et al. 2013). Both the mean and eddy components of the vertical heat advection term have large magnitudes in regions associated with major topographic features, and are generally negligible elsewhere. Because of the cancellation between mean and eddy vertical heat fluxes, the net contribution to the heat budget is small relative to the horizontal advection terms, and likely has been overestimated in studies that do not include eddy heat

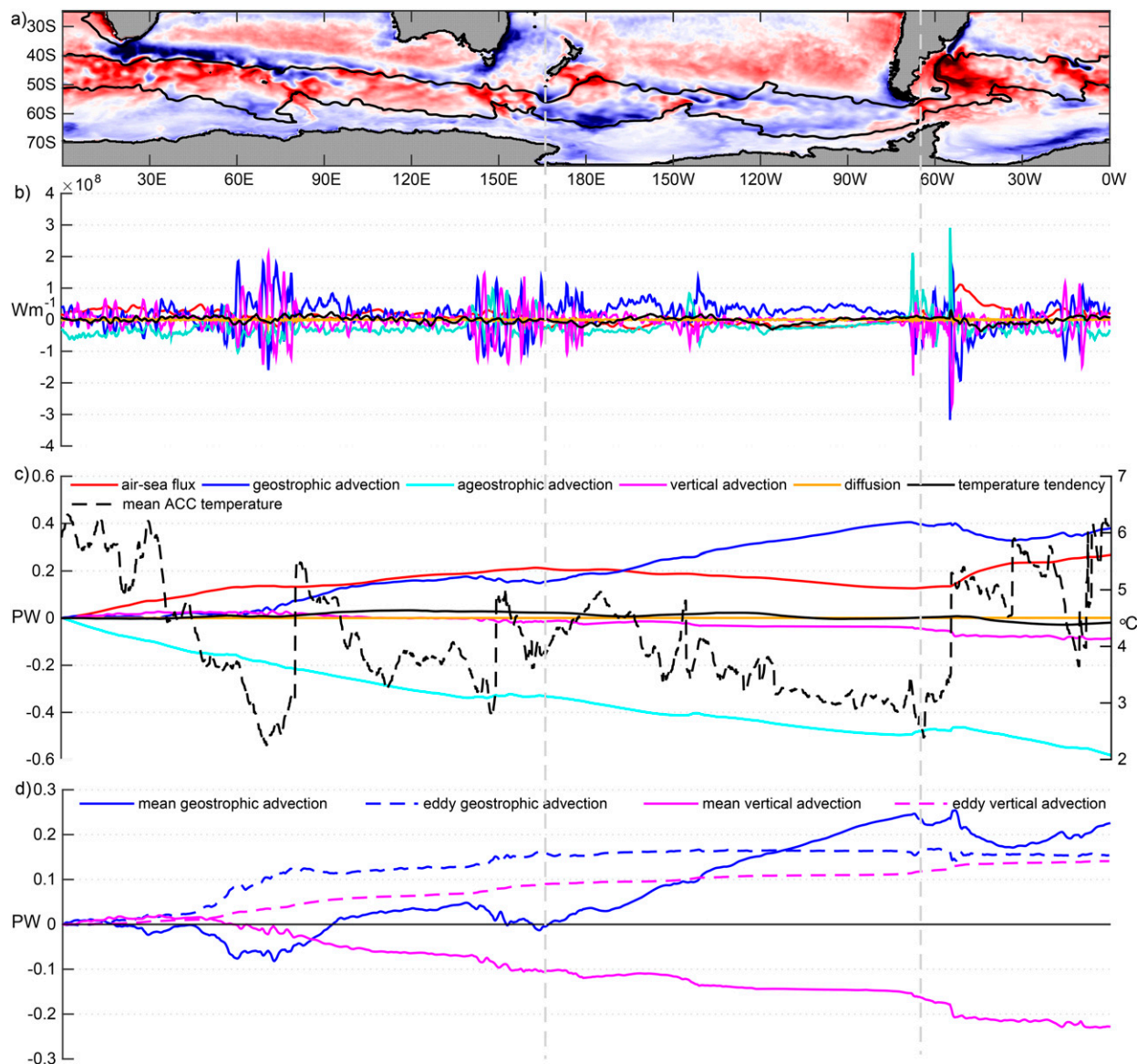


FIG. 4. SOSE vertically and meridionally integrated heat budget solution: (a) 2005–10 mean net air–sea heat flux (colors) with SSH contours defining the northern and southern integration boundaries (solid lines), (b) heat budget terms in Eq. (1) integrated to 624 m and between SSH contours (W m^{-2}), (c) cumulative sum of the terms in (b) in PW as well as the mean temperature averaged vertically in the upper ocean (to 624 m) and between SSH contours in (a) (black dashed line), and (d) cumulative sum of mean and eddy contributions to the geostrophic and vertical advection terms (PW). Gray dashed lines mark Campbell Plateau and Drake Passage, separating the Atlantic/Indian sector from the Pacific sector. Total integrated values are listed in Table 1.

fluxes (Dong et al. 2007). Note that because the heat budget is integrated to a constant depth level rather than an isopycnal, there are vertical displacements in isopycnals along the ACC path that may appear as vertical heat flux, which are not associated with diapycnal vertical velocities, but they are small.

The mean temperature along the ACC path (Fig. 4c, dashed black), averaged vertically and between the two SSH contours shown in Fig. 4a, shows that the ACC is

warmer in the Atlantic/Indian sector and cooler in the Pacific sector. The ACC mean temperature ranges from 6°C in the Atlantic to 3°C in the southeast Pacific. This temperature difference is significant as the temperature variance in the core of the ACC is of the order 1°C in SOSE. This temperature contrast from the Atlantic to the Pacific was previously shown by Sun and Watts (2002) and earlier authors; Sun and Watts (2002) attributed the heat sources to the Brazil Current and the

TABLE 1. SOSE 2005–10 mean heat budget terms (PW) from Eq. (1) integrated over the upper 624 m and between SSH lines as described in section 2 for the entire ACC and the Atlantic/Indian and Pacific sectors separately.

Heat budget term	Total	Atlantic/Indian	Pacific
Air–sea flux	0.27	0.35	−0.08
Geostrophic advection	0.38	0.13	0.25
Mean	0.23	−0.01	0.24
Eddy	0.15	0.14	0.01
Ageostrophic advection	−0.58	−0.42	−0.16
Vertical advection	−0.09	−0.06	−0.03
Mean	−0.23	−0.18	−0.05
Eddy	0.14	0.12	0.02
Diffusion	0	0	0
Temperature tendency	−0.02	0.00	−0.02

Agulhas Return Current, that is, to subtropical western boundary current sources. Although our results are in agreement with Sun and Watts (2002), our results also indicate that horizontal advection in the Atlantic/Indian sector is not solely responsible for the heat content variation along the ACC; air–sea heat fluxes contribute about half of the necessary heat input (Fig. 4c). The temperature difference along the mean path of the ACC also has important implications for the contribution of the mean flow to poleward heat transport in the Southern Ocean as the poleward flowing section of the ACC carries more heat than the equatorward flowing Malvinas Current (Sun and Watts 2002).

The circumpolar integrals of terms shown in Fig. 4, as well as the terms integrated separately over the Atlantic/Indian and Pacific sectors, are listed in Table 1. The circumpolar integral of air–sea flux in the ACC shows 0.27 PW ocean heat gain, which is a result of 0.35 PW of heat gain in the Atlantic/Indian sector and −0.08 PW heat loss in the Pacific sector. As is the case for air–sea heat flux, the sign of the time-mean geostrophic advection term differs between the two regions, with −0.01 PW in the Atlantic/Indian and 0.24 PW in the Pacific. The contributions to the circumpolar integrated horizontal and vertical eddy advection terms are dominated by the Atlantic/Indian sector because this sector captures all of the major eddy-rich topographic features along the ACC path excluding CP and the Pacific–Antarctic Ridge. The circumpolar integral of the geostrophic advection term is 0.38 PW, and 0.27 PW air–sea heat gain is balanced by the sum of −0.58 PW cooling due to the ageostrophic advection term and −0.09 PW cooling due to the total vertical advection term. Thus, in the circumpolar integral, the dominant balance is between the heat gain due to geostrophic advection and air–sea flux terms and the heat loss due to the ageostrophic advection term. However, when integrated over each

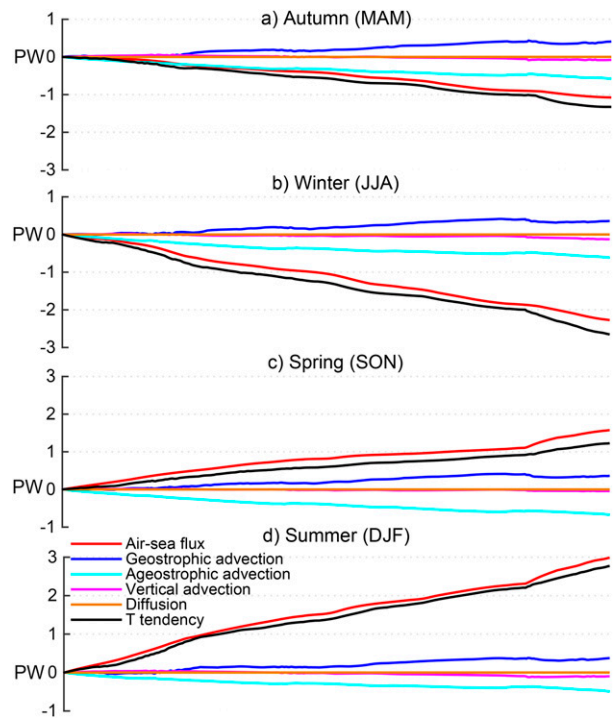


FIG. 5. Cumulatively summed heat budget terms (PW) as in Fig. 4 with each season separately: (a) March–May (MAM), (b) June–August (JJA), (c) September–November (SON), and (d) December–February (DJF). Note that the y axis limits differ for each season to capture the large seasonal cycle in air–sea fluxes.

ocean basin separately, in the Atlantic/Indian sector air–sea heat gain and the eddy component of geostrophic advection balance cooling by the ageostrophic advection term, while in the Pacific sector the mean geostrophic advection term balances cooling by the ageostrophic advection term and air–sea heat loss. The time-mean temperature tendency is small but negative (cooling) over the entire ACC although this signal is confined to the Pacific sector where air–sea flux tends to be negative.

c. Seasonal variability

The time-mean heat budget is the residual of a much larger seasonal cycle, where seasonal variation in temperature tendency is dominated by the seasonal cycle in air–sea heat flux (Fig. 5). The circumpolar integrated ACC air–sea heat flux ranges from −2 PW in winter to 3 PW in summer and on seasonal scales is predominantly balanced by the temperature tendency, with a small negative offset due to net cooling by the sum of the geostrophic, ageostrophic, and vertical advection terms. Notably, the ageostrophic advection term does not show a strong seasonal cycle, differing from a previous observational study (Dong et al. 2007). This difference

in seasonality of the ageostrophic advection term may be attributed to seasonal variations in the mixed layer depth boundary of the mixed layer model of Dong et al. (2007), whereas a constant depth of integration is used in this analysis. Alternatively, variability in the small non-Ekman component of the ageostrophic advection term on nonseasonal time scales may contribute to the lack of clear seasonal variability in ageostrophic advection in SOSE. However, the magnitude of the ageostrophic advection term is slightly larger in winter and spring (Figs. 5c,e), consistent with the seasonal cycle in the strength and position of westerly winds that force the Ekman transport. The magnitude and zonal patterns in the geostrophic and vertical advection terms (Fig. 5) and their corresponding mean and eddy components (not shown) do not show significant seasonal variation, consistent with the conclusion that the spatial variations in the advection terms are related to topographic features and intrinsic ocean variability.

Time series of the 3-month averaged, depth-integrated heat budget integrated in the Atlantic/Indian and Pacific sectors separately (similar to Table 1) demonstrate the large seasonal cycle in temperature tendency that closely follows air–sea heat flux in magnitude and sign but with a slight negative offset as a result of the sum of the seasonal mean advection terms in the budget (Figs. 6a,b). Temporal variations in the seasonally averaged advection terms are relatively small and, unlike air–sea heat flux, the sign of the advective terms remains constant in all seasons. Note that there is substantial variability in the heat budget terms on shorter time scales that is not considered in this analysis. There is a significant difference in the geostrophic advection term between the Atlantic/Indian and Pacific sectors that is of a similar magnitude to the difference in air–sea heat flux (Fig. 6c), but the difference in vertical and ageostrophic advection terms between the two regions is small relative to the standard deviation of these terms. We hypothesize that the mean geostrophic advection term differs spatially due to large-scale differences in the meridional direction of the ACC flow along its circumpolar path, with small divergence of geostrophic temperature advection in the Atlantic/Indian where the ACC flows equatorward and convergence of geostrophic temperature advection in the Pacific sector where the ACC mean flow is poleward. This zonal difference in geostrophic heat transport is mostly compensated by the zonal difference in air–sea heat flux, leading to only a small temperature tendency difference between the two regions. The next section is devoted to exploring the physical explanation for the zonal variation in geostrophic advection and heat flux along the ACC in more detail.

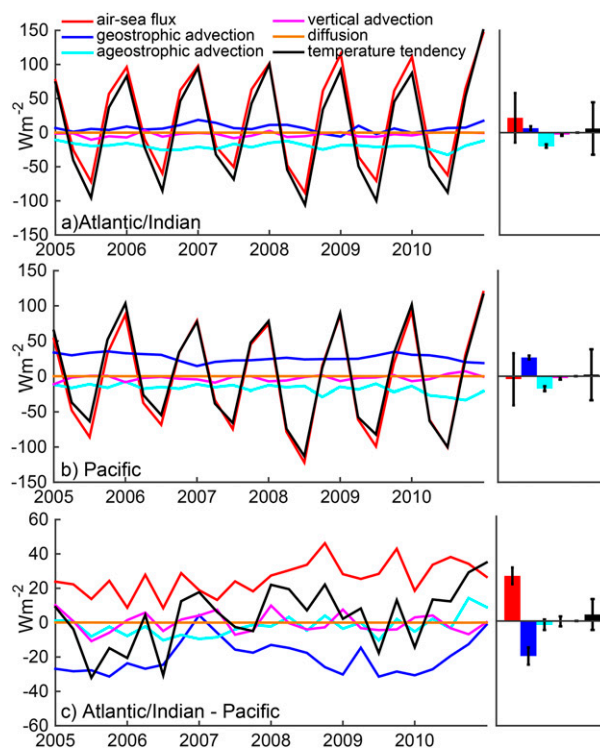


FIG. 6. Time series of seasonal (3 month) integrated (left) heat budget terms (W m^{-2}) and (right) time-mean terms with error bars indicating one standard deviation above and below the mean for the average of (a) the Atlantic/Indian sector of the ACC and (b) the Pacific sector of the ACC, and (c) the difference between (a) and (b).

d. The role of geostrophic advection in the ACC heat budget

Poleward flowing western boundary currents and their extensions are sites of intense ocean heat loss as mean geostrophic advection brings warm, subtropical water poleward under a colder atmosphere (Vivier et al. 2002; Dong and Kelly 2004). The Pacific sector of the ACC is analogous to a western boundary current extension, as the mean geostrophic transport of the ACC is poleward as it enters the Pacific, transporting ACC water under a colder atmosphere, causing large turbulent (latent and sensible) heat losses. The ACC then veers sharply equatorward in the Malvinas Current after passing through Drake Passage, under a relatively warm atmosphere where there is a minimum in turbulent heat loss, resulting in net heat flux into the ocean. To demonstrate the similarities between the poleward flowing ACC in the Pacific sector and poleward-flowing western boundary current extensions, particularly the ARC, it is useful to compare and contrast the heat budget in these two regions.

Figure 7 shows the time-mean integrated heat budget solution in the ARC region similar to that shown in

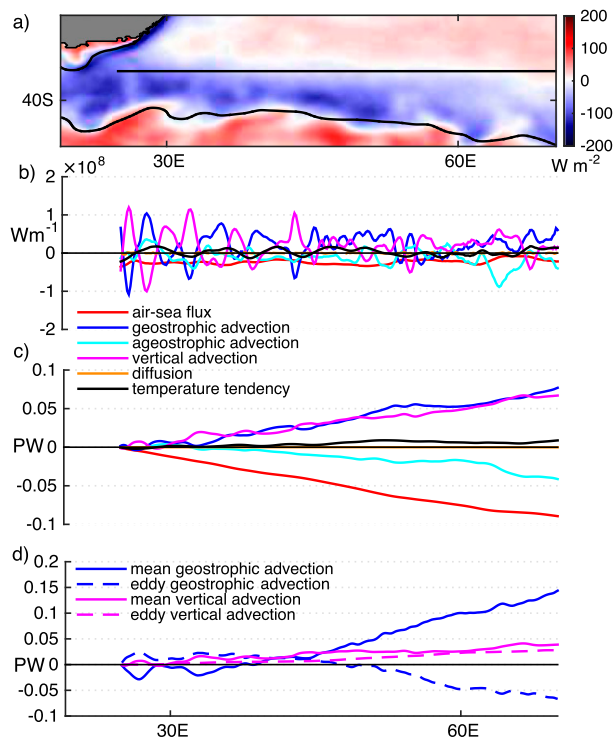


FIG. 7. Integrated heat budget terms similar to Fig. 4 for the Agulhas Return Current (ARC) cooling region: (a) air-sea heat flux in the ARC region; black lines show the SSH contour used as the southern boundary and a line of constant latitude used as the northern boundary to integrate the heat budget terms in Eq. (1), (b) heat budget terms in Eq. (1) integrated to 624 m and between meridional contours shown in (a) (W m^{-1}), (c) cumulative sum of heat budget terms integrated to 624 m and between bounds in (a), and (d) cumulative sum of mean and eddy contributions to the geostrophic and vertical advection terms.

Fig. 4 for the ACC. The convergence of geostrophic and vertical temperature advection is balanced mainly by ocean heat loss, with a smaller contribution from the ageostrophic advection term (Fig. 7c). This balance is consistent with previous analyses of the heat budget in western boundary currents that show that geostrophic advection is balanced by heat loss to the atmosphere (Dong and Kelly 2004; Roemmich et al. 2005). Decomposition of horizontal and vertical advection into the mean and eddy components (Fig. 7d) shows that the horizontal geostrophic advection term is the largest positive term, bringing warm subtropical water into the region. However, the eddy component of the geostrophic advection term is negative, leading to substantial cancellation between the mean and eddy contributions to the total geostrophic advection term. Both the mean and eddy vertical advection terms are positive in the ARC, which differs from the ACC because wind stress curl drives downwelling of warmer surface water rather than upwelling at this latitude. The ARC heat balance is

similar to the dominant balance in the Pacific sector of the ACC (Fig. 4c), where mean geostrophic advection warms the upper ocean and is balanced by cooling from both air-sea fluxes and Ekman advection. There are a few other differences between the ARC and the Pacific sector of the ACC: air-sea heat loss is the dominant cooling term in the ARC, whereas in the Pacific sector of the ACC cooling by the Ekman advection term is larger than the air-sea heat loss term. Also, both mean and eddy vertical advection contribute to net warming in the ARC, whereas in the Pacific sector of the ACC the vertical advection term is negative with substantial cancellation between the time-mean and eddy components (Fig. 4d). Given the difference in vertical temperature structure and stronger Ekman transport in the ACC, these differences are unsurprising.

Time series of the ARC (not shown) indicate that there is large variability in the geostrophic and ageostrophic advection terms, unlike in the ACC where the temperature tendency is mostly balanced by air-sea fluxes on seasonal time scales (Fig. 6d). The variability in the geostrophic advection term in the ARC is dominated by large nonseasonal variations in the transport and recirculations in the current, obscuring the seasonal cycle. The resulting temperature tendency averaged over the entire ARC has a less pronounced seasonal cycle than in the ACC. In this highly energetic region, the quantitative heat budget results are only weakly sensitive to the boundaries of integration but the sign of the integrated terms does not change and the qualitative result remains consistent. While the role of geostrophic advection in the time-averaged heat budget is similar in the ARC and the Pacific sector of the ACC, the temporal variability in the geostrophic advection term in the ARC is much larger than in the ACC, unsurprising given the large variability in transport due to recirculations in the ARC.

4. Summary and conclusions

We have analyzed the three-dimensional spatial variations and seasonal variability in the upper ocean heat budget of the Antarctic Circumpolar Current (ACC) in the Southern Ocean State Estimate (SOSE) for the years 2005–10. SOSE is eddy permitting, well constrained by ocean observations in the top 2000 m of the ocean, and has closed budgets, providing new insights into the heat budget in the Southern Ocean compared to the previous studies of the heat budget that have been limited by sparse observations, unresolved mesoscale processes, and inadequate surface heat fluxes, leading to large imbalances in the heat budget (Dong et al. 2007). The circumpolar integrated heat budget in the ACC in

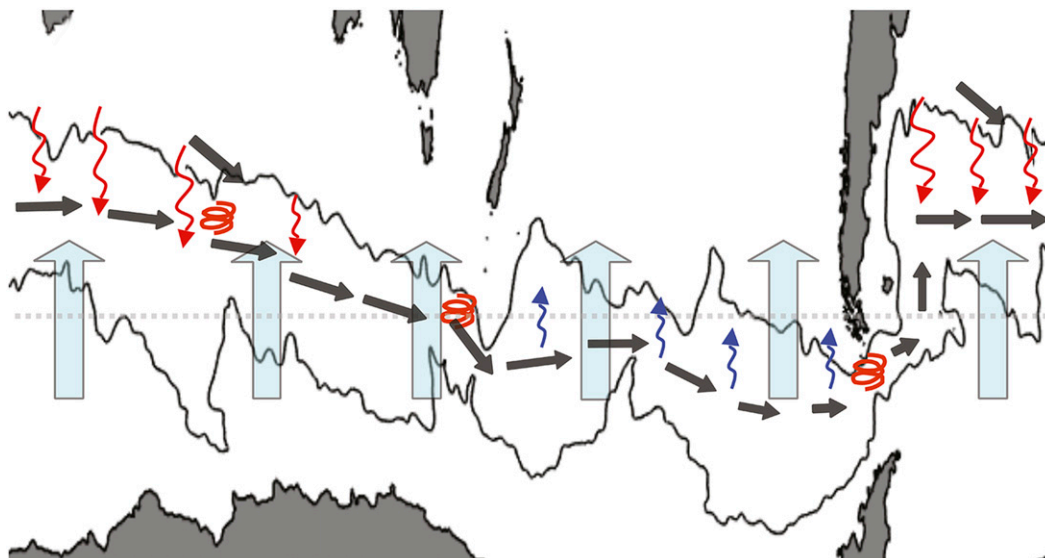


FIG. 8. Schematic showing variations in the upper ocean heat budget along the ACC. Black lines are the SSH contours used as northern and southern boundaries of the ACC in this study. The dashed gray line marks the mean latitude of the ACC. Red and blue arrows indicate ocean heat gain and heat loss; large cyan arrows indicate cooling by divergence of Ekman temperature transport; dark gray arrows indicate the relative magnitude of the mean horizontal geostrophic transport, showing convergence in the Pacific sector and transport of subtropical water into the ACC from the ARC in the Indian sector and from the Brazil Current in the Atlantic sector; and red spirals indicate warming due to divergence of eddy heat flux associated with major topographic features.

SOSE shows 0.27 PW of ocean heat gain from the atmosphere and 0.38 PW heat gain from divergence of geostrophic temperature advection are balanced by -0.58 PW cooling by divergence of Ekman temperature advection and -0.09 PW divergence of vertical temperature advection. A summary of the dominant heat budget processes is shown in Fig. 8. Our principal conclusions are the following:

- Large-scale patterns of air–sea heat fluxes from SOSE agree with the most recent heat flux products (Large and Yeager 2009; Cerovečki et al. 2011), showing a robust zonally asymmetric pattern in the ACC, with ocean heat gain in the Atlantic/Indian sector and ocean heat loss in the Pacific sector.
- In the Atlantic/Indian sector of the ACC, 0.35 PW of surface ocean heat gain is opposed by -0.42 PW cooling by divergence of ageostrophic heat advection due to Ekman transport, consistent with Dong et al. (2007) and Sallée et al. (2006). The 0.14 PW warming due to divergence of geostrophic eddy heat flux and -0.06 PW cooling due to divergence of vertical heat advection play a lesser role.
- In the Pacific sector of the ACC, both the -0.08 PW ocean heat loss to the atmosphere and the -0.16 PW cooling by the divergence of ageostrophic heat advection due to Ekman transport are mainly balanced by 0.25 PW convergence of geostrophic heat advection.

The warming by divergence of geostrophic heat advection is achieved almost entirely by the mean geostrophic flow, unlike in the Atlantic/Indian sector where the mean component is insignificant and instead is dominated by eddy heat flux divergence associated with major topographic features.

- Comparison of the ACC heat budget with the poleward-flowing, subtropical Agulhas Return Current (ARC) suggests that the dominant heat balance in the Pacific sector of the ACC is similar to that in the ARC and other poleward flowing western boundary current extensions.
- Divergence of both horizontal and vertical transient eddy heat flux causes significant warming in narrow regions associated with major topographic features with enhanced mesoscale energy (e.g., Naveira Garabato et al. 2011).
- The seasonal cycle in air–sea heat flux has a magnitude of 200 W m^{-2} and is predominantly balanced by the seasonal cycle of temperature tendency, while the divergence of temperature advection does not show a distinct seasonal cycle.

We have demonstrated that mean geostrophic temperature advection is a dominant component of the Southern Ocean heat budget due to meridional standing meanders of the ACC and to a lesser extent the

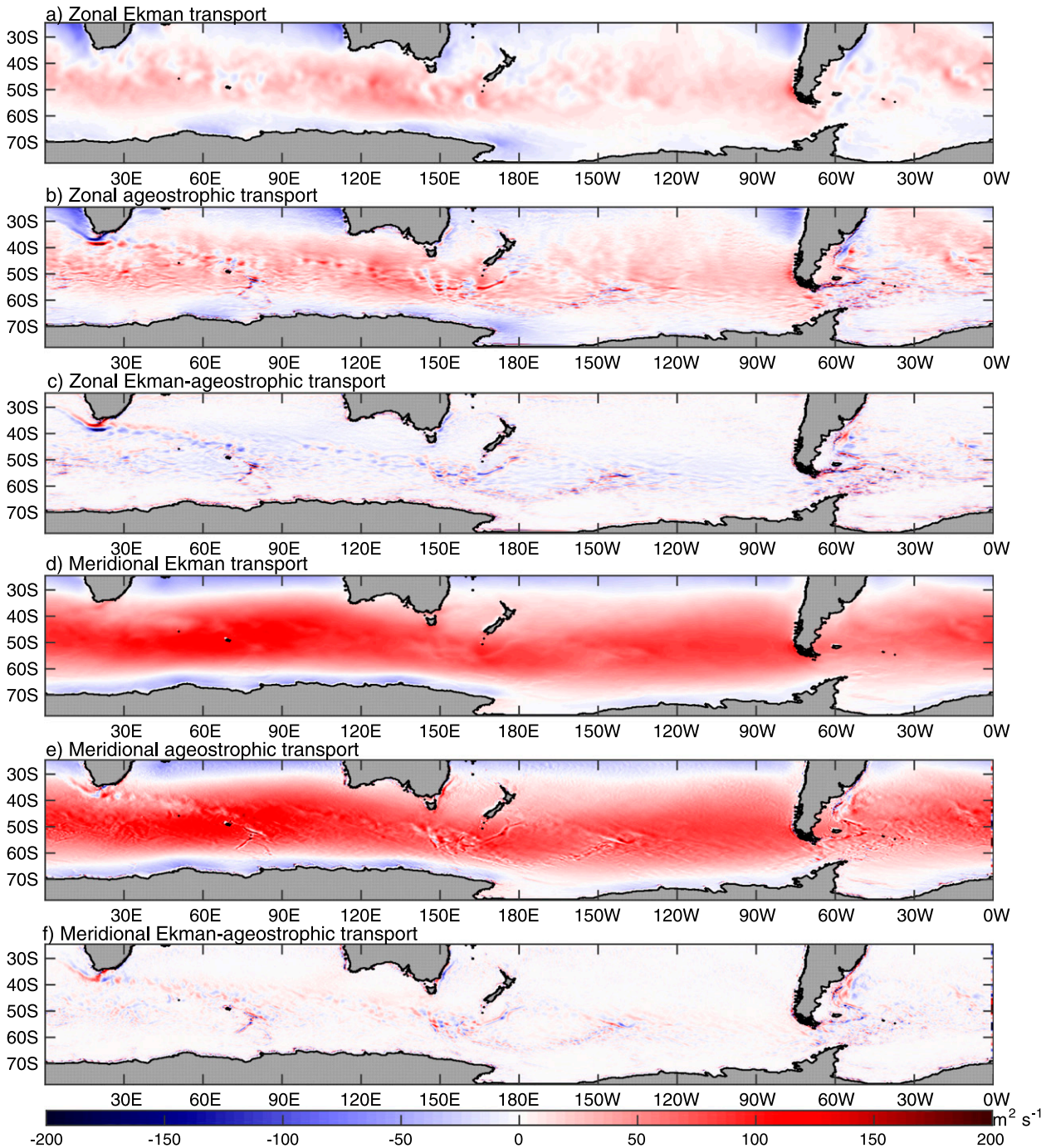


FIG. A1. Comparison between Ekman transport calculated from SOSE wind stress fields and ageostrophic transport calculated from the residual between total and geostrophic velocities integrated vertically over the Ekman layer. (a) Zonal Ekman transport, (b) zonal ageostrophic transport, (c) difference between zonal Ekman transport and zonal ageostrophic transport, (d) meridional Ekman transport, (e) meridional ageostrophic transport, and (f) difference between meridional Ekman transport and meridional ageostrophic transport.

inflow of warm, subtropical boundary current waters into the ACC across the Subantarctic Front (Fig. 8). This result supports the inference of Sun and Watts (2002) that since heat content varies along the mean ACC path there must be an associated net poleward

heat transport. Sun and Watts (2002) concluded that subtropical water, particularly from the Brazil–Malvinas Confluence, is responsible for the variation in heat content along the ACC mean path. Our results indicate that air–sea heat flux is also a major source of

heat to the ACC mean flow in the Atlantic/Indian sector; this difference is likely due to availability of modern flux products that were not available to Sun and Watts (2002). The atmosphere above the Southern Ocean is more zonally uniform than the ocean because it lacks the strong topographic control that steers the ACC meridionally over a 10° latitude range. The ACC gains heat from the atmosphere when it flows northward in the Malvinas Current and throughout the Indian and Atlantic sectors, in addition to advective ocean heat input by the Brazil Current and ARC, and releases some of this heat back to the atmosphere as it flows southward in the Pacific (Fig. 8). This phenomenon is analogous to the heat exchange by horizontal gyre circulations, and we have shown that the ACC budget in the Pacific is similar to the budget in the ARC and other western boundary current extensions where relatively warm waters are advected poleward. Perturbation experiments in SOSE or other models would help to elucidate the physical mechanism linking geostrophic advection and air–sea heat flux, but are beyond the scope of this study.

The dominant role of northward Ekman transport in the heat budget is indicative of the surface branch of the upper cell of the Southern Ocean overturning circulation, with ocean heat gain throughout the Atlantic/Indian sector transforming Antarctic Surface Water to lighter water as it is advected equatorward. Instead, in the Pacific where the net heat flux is weakly negative, freshwater fluxes must achieve the surface buoyancy gain necessary to close the upper cell of the overturning circulation. Although the full buoyancy budget is beyond the scope of this study, the striking asymmetry in air–sea heat flux presented here is also present in the total buoyancy flux in the Southern Ocean (Cerovečki et al. 2013; Radko and Marshall 2006). Further work is needed to investigate the impact of this asymmetric buoyancy forcing on the strength and structure of the overturning circulation, expanding on the idealized model presented by Radko and Marshall (2006).

Our results have important implications for climate models; they imply that models must have accurate spatial correlations between mean velocity and temperature fields in order to simulate the poleward heat flux by the ACC. Low-resolution models that approximate the total ACC volume transport well but lack the narrow, intense jets and meandering structure of the current may be misrepresenting heat transport by the mean ACC flow (e.g., Dufour et al. 2012). Additionally, models that do not resolve eddies accurately lack the important contribution of warming by divergence of eddy heat flux to the heat budget in

regions near major topographic features. While SOSE at $1/6^\circ$ resolves the ACC jet structure better than global coarse-resolution models, there are unresolved finer-scale processes that may alter the mean geostrophic heat flux. Further work is needed with the next generation of higher-resolution products to explore the impact of model resolution on mean ACC heat transport.

Because of the importance of air–sea heat and freshwater fluxes in determining the strength of the upper cell of the overturning circulation (Radko and Marshall 2006), the pronounced zonal asymmetry in the ACC heat budget shown in this work illustrates the need for further work to understand the three-dimensional structure of the overturning circulation in the Southern Ocean. Understanding how observed and predicted future changes in buoyancy forcing will alter the strength of the overturning circulation is a necessary step toward understanding the role of the Southern Ocean in future uptake and storage of heat, carbon, and nutrients.

Acknowledgments. V. Tamsitt, L. D. Talley, and I. Cerovečki were supported by NSF Grant OCE1357072. M. R. Mazloff acknowledges support from NSF Grant PLR1425989. Computational resources for the Southern Ocean State Estimate were provided by NSF XSEDE resource Grant OCE130007. The SOSE iteration 100 solution is freely available for download (<http://sose.ucsd.edu>). We thank two anonymous reviewers for comments that improved the quality of this manuscript.

APPENDIX

Comparison between Ekman Transport from Winds and Ageostrophic Transport

Here we briefly show a comparison between Ekman transport calculated from wind stress and ageostrophic transport calculated from the residual between total and geostrophic velocities in the Southern Ocean state estimate. The components of Ekman transport U_{ek} and V_{ek} ($m^2 s^{-1}$) integrated over the Ekman depth d_{ek} are estimated from the SOSE zonal and meridional mean wind stress fields, $\bar{\tau}^x$ and $\bar{\tau}^y$, according to the relations $U_{ek} = \bar{\tau}^y/(\rho f)$ and $V_{ek} = \bar{\tau}^x/(\rho f)$, where ρ is the density and f is the Coriolis parameter. The ageostrophic transport U_{ag} is estimated by taking the difference between the total velocity u and the geostrophic velocity calculated from the SOSE pressure field u_g and integrating vertically from the surface to d_{ek} such that $U_{ag} = \int_{-d_{ek}}^0 (u - u_g) dz$. For this comparison we assume a constant Ekman depth of 100 m, based on observations of Ekman transport in the Drake Passage (Lenn and Chereskin 2009); however, the qualitative difference

between the Ekman and ageostrophic transports is not sensitive to this choice.

Figure A1 shows the 1) zonal Ekman transport from wind stress, 2) zonal ageostrophic transport, 3) zonal Ekman transport minus zonal ageostrophic transport, 4) meridional Ekman transport from wind stress, 5) meridional ageostrophic transport, and 6) meridional Ekman transport minus meridional ageostrophic transport. Differences between the zonal and meridional components of Ekman transport and ageostrophic transport are concentrated in energetic regions, particularly western boundary currents and close to major topographic features where ageostrophic transport due to processes other than Ekman transport are expected. These differences are noisy and do not have a sign preference. Thus when the ageostrophic advection is integrated meridionally and zonally, the non-Ekman contributions are not significant and the ageostrophic transport is a good approximation to the Ekman transport.

REFERENCES

- Bourassa, M. A., and Coauthors, 2013: High-latitude ocean and sea ice surface fluxes: Challenges for climate research. *Bull. Amer. Meteor. Soc.*, **94**, 403–423, doi:[10.1175/BAMS-D-11-00244.1](https://doi.org/10.1175/BAMS-D-11-00244.1).
- Cerovečki, I., M. R. Mazloff, and L. D. Talley, 2011: A comparison of Southern Ocean air–sea buoyancy flux from an ocean state estimate with five other products. *J. Climate*, **24**, 6283–6306, doi:[10.1175/2011JCLI3858.1](https://doi.org/10.1175/2011JCLI3858.1).
- , L. D. Talley, M. R. Mazloff, and G. Maze, 2013: Subantarctic Mode Water formation, destruction, and export in the eddy-permitting Southern Ocean state estimate. *J. Phys. Oceanogr.*, **43**, 1485–1511, doi:[10.1175/JPO-D-12-0121.1](https://doi.org/10.1175/JPO-D-12-0121.1).
- Chelton, D. B., M. G. Schlax, D. L. Witter, and J. G. Richman, 1990: *Geosat* altimeter observations of the surface circulation of the Southern Ocean. *J. Geophys. Res.*, **95** (C10), 17 877–17 903, doi:[10.1029/JC095iC10p17877](https://doi.org/10.1029/JC095iC10p17877).
- , R. Deszoeke, M. G. Schlax, K. El Naggar, and N. Siwertz, 1998: Geographical variability of the first baroclinic Rossby radius of deformation. *J. Phys. Oceanogr.*, **28**, 433–460, doi:[10.1175/1520-0485\(1998\)028<0433:GVOTFB>2.0.CO;2](https://doi.org/10.1175/1520-0485(1998)028<0433:GVOTFB>2.0.CO;2).
- Dee, D. P., and Coauthors, 2011: The ERA-Interim reanalysis: Configuration and performance of the data assimilation system. *Quart. J. Roy. Meteor. Soc.*, **137**, 553–597, doi:[10.1002/qj.828](https://doi.org/10.1002/qj.828).
- Dong, S., and K. A. Kelly, 2004: Heat budget in the Gulf Stream region: The importance of heat storage and advection. *J. Phys. Oceanogr.*, **34**, 1214–1231, doi:[10.1175/1520-0485\(2004\)034<1214:HBITGS>2.0.CO;2](https://doi.org/10.1175/1520-0485(2004)034<1214:HBITGS>2.0.CO;2).
- , S. T. Gille, and J. Sprintall, 2007: An assessment of the Southern Ocean mixed layer heat budget. *J. Climate*, **20**, 4425–4442, doi:[10.1175/JCLI4259.1](https://doi.org/10.1175/JCLI4259.1).
- Dufour, C. O., L. L. Sommer, J. D. Zika, M. Gehlen, J. C. Orr, P. Mathiot, and B. Barnier, 2012: Standing and transient eddies in the response of the Southern Ocean meridional overturning to the southern annular mode. *J. Climate*, **25**, 6958–6974, doi:[10.1175/JCLI-D-11-00309.1](https://doi.org/10.1175/JCLI-D-11-00309.1).
- Faure, V., M. Arhan, S. Speich, and S. Gladyshev, 2011: Heat budget of the surface mixed layer south of Africa. *Ocean Dyn.*, **61**, 1441–1458, doi:[10.1007/s10236-011-0444-1](https://doi.org/10.1007/s10236-011-0444-1).
- Fenty, I., and P. Heimbach, 2013: Coupled sea ice–ocean state estimation in the Labrador Sea and Baffin Bay. *J. Phys. Oceanogr.*, **43**, 884–904, doi:[10.1175/JPO-D-12-065.1](https://doi.org/10.1175/JPO-D-12-065.1).
- Forget, G., 2010: Mapping ocean observations in a dynamical framework: A 2004–06 ocean atlas. *J. Phys. Oceanogr.*, **40**, 1201–1221, doi:[10.1175/2009JPO4043.1](https://doi.org/10.1175/2009JPO4043.1).
- Gille, S., and K. Kelly, 1996: Scales of spatial and temporal variability in the Southern Ocean. *J. Geophys. Res.*, **101**, 8759–8773, doi:[10.1029/96JC00203](https://doi.org/10.1029/96JC00203).
- Hobbs, W. R., and M. N. Raphael, 2007: A representative time-series for the Southern Hemisphere zonal wave 1. *Geophys. Res. Lett.*, **34**, L05702, doi:[10.1029/2006GL028740](https://doi.org/10.1029/2006GL028740).
- , and —, 2010: Characterizing the zonally asymmetric component of the SH circulation. *Climate Dyn.*, **35**, 859–873, doi:[10.1007/s00382-009-0663-z](https://doi.org/10.1007/s00382-009-0663-z).
- Ito, T., M. Woloszyn, and M. Mazloff, 2010: Anthropogenic carbon dioxide transport in the Southern Ocean driven by Ekman flow. *Nature*, **463**, 80–83, doi:[10.1038/nature08687](https://doi.org/10.1038/nature08687).
- Iudicone, D., G. Madec, and T. J. McDougall, 2008: Water-mass transformations in a neutral density framework and the key role of light penetration. *J. Phys. Oceanogr.*, **38**, 1357–1376, doi:[10.1175/2007JPO3464.1](https://doi.org/10.1175/2007JPO3464.1).
- Jerlov, N. G., 1968: *Optical Oceanography*. Elsevier, 199 pp.
- Karsten, R. H., and J. Marshall, 2002: Constructing the residual circulation of the ACC from observations. *J. Phys. Oceanogr.*, **32**, 3315–3327, doi:[10.1175/1520-0485\(2002\)032<3315:CTRCOT>2.0.CO;2](https://doi.org/10.1175/1520-0485(2002)032<3315:CTRCOT>2.0.CO;2).
- Large, W. G., and S. G. Yeager, 2009: The global climatology of an interannually varying air–sea flux data set. *Climate Dyn.*, **33**, 341–364, doi:[10.1007/s00382-008-0441-3](https://doi.org/10.1007/s00382-008-0441-3).
- , J. C. McWilliams, and S. C. Doney, 1994: Oceanic vertical mixing: A review and a model with a nonlocal boundary layer parameterization. *Rev. Geophys.*, **32**, 363–403, doi:[10.1029/94RG01872](https://doi.org/10.1029/94RG01872).
- Lenn, Y.-D., and T. K. Chereskin, 2009: Observations of Ekman currents in the Southern Ocean. *J. Phys. Oceanogr.*, **39**, 768–779, doi:[10.1175/2008JPO3943.1](https://doi.org/10.1175/2008JPO3943.1).
- Marshall, J., and T. Radko, 2003: Residual-mean solutions for the Antarctic Circumpolar Current and its associated overturning circulation. *J. Phys. Oceanogr.*, **33**, 2341–2354, doi:[10.1175/1520-0485\(2003\)033<2341:RSFTAC>2.0.CO;2](https://doi.org/10.1175/1520-0485(2003)033<2341:RSFTAC>2.0.CO;2).
- , A. Adcroft, C. Hill, L. Perelman, and C. Heisey, 1997: A finite-volume, incompressible Navier Stokes model for studies of the ocean on parallel computers. *J. Geophys. Res.*, **102** (C3), 5753–5766, doi:[10.1029/96JC02775](https://doi.org/10.1029/96JC02775).
- Mazloff, M. R., P. Heimbach, and C. Wunsch, 2010: An eddy-permitting Southern Ocean state estimate. *J. Phys. Oceanogr.*, **40**, 880–899, doi:[10.1175/2009JPO4236.1](https://doi.org/10.1175/2009JPO4236.1).
- Milliff, R. F., T. J. Hoar, H. van Loon, and M. Raphael, 1999: Quasi-stationary wave variability in NSCAT winds. *J. Geophys. Res.*, **104**, 11 425–11 435, doi:[10.1029/1998JC900087](https://doi.org/10.1029/1998JC900087).
- Morrison, A. K., A. M. Hogg, and M. L. Ward, 2011: Sensitivity of the Southern Ocean overturning circulation to surface buoyancy forcing. *Geophys. Res. Lett.*, **38**, L14602, doi:[10.1029/2011GL048031](https://doi.org/10.1029/2011GL048031).
- , O. A. Saenko, A. M. Hogg, and P. Spence, 2013: The role of vertical eddy flux in Southern Ocean heat uptake. *Geophys. Res. Lett.*, **40**, 5445–5450, doi:[10.1002/2013GL057706](https://doi.org/10.1002/2013GL057706).
- Naveira Garabato, A. C., R. Ferrari, and K. L. Polzin, 2011: Eddy stirring in the Southern Ocean. *J. Geophys. Res.*, **116**, C09019, doi:[10.1029/2010JC006818](https://doi.org/10.1029/2010JC006818).
- Paulson, C. A., and J. J. Simpson, 1977: Irradiance measurements in the upper ocean. *J. Phys. Oceanogr.*, **7**, 952–956, doi:[10.1175/1520-0485\(1977\)007<0952:IMITUO>2.0.CO;2](https://doi.org/10.1175/1520-0485(1977)007<0952:IMITUO>2.0.CO;2).

- Radko, T., and J. C. Marshall, 2006: The Antarctic Circumpolar Current in three dimensions. *J. Phys. Oceanogr.*, **36**, 651–669, doi:[10.1175/JPO2893.1](https://doi.org/10.1175/JPO2893.1).
- Rintoul, S. R., and M. H. England, 2002: Ekman transport dominates local air–sea fluxes in driving variability of Subantarctic Mode Water. *J. Phys. Oceanogr.*, **32**, 1308–1321, doi:[10.1175/1520-0485\(2002\)032<1308:ETDLAS>2.0.CO;2](https://doi.org/10.1175/1520-0485(2002)032<1308:ETDLAS>2.0.CO;2).
- Rocha, C. B., T. K. Chereskin, S. T. Gille, and D. Menemenlis, 2016: Mesoscale to submesoscale wavenumber spectra in Drake Passage. *J. Phys. Oceanogr.*, **46**, 601–620, doi:[10.1175/JPO-D-15-0087.1](https://doi.org/10.1175/JPO-D-15-0087.1).
- Roemmich, D., J. Gilson, J. Willis, P. Sutton, and K. Ridgway, 2005: Closing the time-varying mass and heat budgets for large ocean areas: The Tasman box. *J. Climate*, **18**, 2330–2343, doi:[10.1175/JCLI3409.1](https://doi.org/10.1175/JCLI3409.1).
- Sallée, J.-B., K. Speer, R. Morrow, and N. Wienders, 2006: Formation of Subantarctic Mode Water in the southeastern Indian Ocean. *Ocean Dyn.*, **56**, 525–542, doi:[10.1007/s10236-005-0054-x](https://doi.org/10.1007/s10236-005-0054-x).
- , R. Morrow, and K. Speer, 2008: Eddy heat diffusion and Subantarctic Mode Water formation. *Geophys. Res. Lett.*, **35**, L05607, doi:[10.1029/2007GL032827](https://doi.org/10.1029/2007GL032827).
- , K. G. Speer, and S. R. Rintoul, 2010: Zonally asymmetric response of the Southern Ocean mixed-layer depth to the southern annular mode. *Nat. Geosci.*, **3**, 273–279, doi:[10.1038/ngeo812](https://doi.org/10.1038/ngeo812).
- Sarmiento, J. L., N. Gruber, M. A. Brzezinski, and J. P. Dunne, 2004: High-latitude controls of thermocline nutrients and low latitude biological productivity. *Nature*, **427**, 56–60, doi:[10.1038/nature02127](https://doi.org/10.1038/nature02127).
- Sloyan, B. M., and S. R. Rintoul, 2001: Circulation, renewal, and modification of Antarctic Mode and Intermediate Water. *J. Phys. Oceanogr.*, **31**, 1005–1030, doi:[10.1175/1520-0485\(2001\)031<1005:CRAMOA>2.0.CO;2](https://doi.org/10.1175/1520-0485(2001)031<1005:CRAMOA>2.0.CO;2).
- Sokolov, S., and S. R. Rintoul, 2009: Circumpolar structure and distribution of the Antarctic Circumpolar Current fronts: 2. Variability and relationship to sea surface height. *J. Geophys. Res.*, **114**, C11019, doi:[10.1029/2008JC005248](https://doi.org/10.1029/2008JC005248).
- Speer, K., S. R. Rintoul, and B. Sloyan, 2000: The diabatic Deacon cell. *J. Phys. Oceanogr.*, **30**, 3212–3222, doi:[10.1175/1520-0485\(2000\)030<3212:TDDC>2.0.CO;2](https://doi.org/10.1175/1520-0485(2000)030<3212:TDDC>2.0.CO;2).
- Sun, C., and D. R. Watts, 2002: Heat flux carried by the Antarctic Circumpolar Current mean flow. *J. Geophys. Res.*, **107** (C9), 3119, doi:[10.1029/2001JC001187](https://doi.org/10.1029/2001JC001187).
- Thompson, A. F., and J.-B. Sallée, 2012: Jets and topography: Jet transitions and the impact on transport in the Antarctic Circumpolar Current. *J. Phys. Oceanogr.*, **42**, 956–972, doi:[10.1175/JPO-D-11-0135.1](https://doi.org/10.1175/JPO-D-11-0135.1).
- van Loon, H., and R. L. Jenne, 1972: The zonal harmonic standing waves in the Southern Hemisphere. *J. Geophys. Res.*, **77**, 992–1003, doi:[10.1029/JC077i006p00992](https://doi.org/10.1029/JC077i006p00992).
- Vivier, F., K. A. Kelly, and L. A. Thompson, 2002: Heat budget in the Kuroshio Extension region: 1993–99. *J. Phys. Oceanogr.*, **32**, 3436–3454, doi:[10.1175/1520-0485\(2002\)032<3436:HBITKE>2.0.CO;2](https://doi.org/10.1175/1520-0485(2002)032<3436:HBITKE>2.0.CO;2).
- , D. Iudicone, F. Busdraghi, and Y.-H. Park, 2010: Dynamics of sea-surface temperature anomalies in the Southern Ocean diagnosed from a 2D mixed-layer model. *Climate Dyn.*, **34**, 153–184, doi:[10.1007/s00382-009-0724-3](https://doi.org/10.1007/s00382-009-0724-3).
- Wang, J., M. R. Mazloff, and S. T. Gille, 2014: Pathways of the Agulhas waters poleward of 29°S. *J. Geophys. Res. Oceans*, **119**, 4234–4250, doi:[10.1002/2014JC010049](https://doi.org/10.1002/2014JC010049).
- Wolfe, C. L., P. Cessi, J. L. McClean, and M. E. Maltrud, 2008: Vertical heat transport in eddying ocean models. *Geophys. Res. Lett.*, **35**, L23605, doi:[10.1029/2008GL036138](https://doi.org/10.1029/2008GL036138).
- Wunsch, C., and P. Heimbach, 2013: Dynamically and kinematically consistent global ocean circulation and ice state estimates. *Int. Geophys.*, **103**, 553–579, doi:[10.1016/B978-0-12-391851-2.00021-0](https://doi.org/10.1016/B978-0-12-391851-2.00021-0).
- Yu, L., and R. A. Weller, 2007: Objectively analyzed air–sea heat fluxes for the global ice-free oceans (1981–2005). *Bull. Amer. Meteor. Soc.*, **88**, 527–539, doi:[10.1175/BAMS-88-4-527](https://doi.org/10.1175/BAMS-88-4-527).